Nanoscale

ROYAL SOCIETY
OF CHEMISTRY

PAPER
Shilong Chen, Malte Behrens *et al.*
Support effect on Ni-based mono- and bimetallic catalysts
in CO_2 hydrogenation

NCNST

Check for updates

Support effect on Ni-based mono- and bimetallic catalysts in CO$_2$ hydrogenation†

Jihao Wang,[a] Shilong Chen, ID *[a] Pierfrancesco Ticali, ID [a] Paulina Summa,[b] Simon Mai,[a] Katarzyna Skorupska ID [b] and Malte Behrens ID *[a]

Aiming at a comprehensive understanding of support effects on Ni-based bimetallic catalyst for CO$_2$ hydrogenation, spectroscopy (DRIFTS) with CO as a probe molecule and temperature-programmed techniques were used to investigate the impact of different supports (MgO, CeO$_2$, ZrO$_2$) on Ni- and Ni,Fe catalysts. Kinetic parameters revealed that the higher selectivity to methanation for Ni and Ni,Fe supported on the reducible oxides (CeO$_2$, ZrO$_2$) is due to the inhibition of reverse water-gas shift reaction (RWGS) by hydrogen. A promoting effect of Fe on Ni was only observed on MgO-supported catalysts. In situ DRIFTS with CO adsorption showed different electronic properties of Ni sites with partially reduced oxide (*i.e.* ZrO$_2$ and CeO$_2$). H$_2$-TPR and CO$_2$-TPD confirmed the significant role of metal-support interaction (MSI) in CeO$_2$-supported catalysts for CO$_2$ activation. The MSI between Ni/Ni,Fe and reducible supports are crucial for catalytic performance, ultimately leading to the higher activity and stability in CO$_2$ hydrogenation.

1. Introduction

CO$_2$ hydrogenation is a cornerstone of sustainable "power-to-gas (P2G)" concepts[1–5] and supported Ni catalysts are considered as the most promising base metal catalyst towards methanation due to their outstanding catalytic performance and low cost.[6–10] Despite the long history of research on nickel-based catalysts, there is still a need for a better fundamental understanding and for further rational optimization of such methanation catalysts.[11,12]

One the one hand, regarding catalyst composition variation or promotion, partial substitution of Ni by a second metal was shown to improve the catalytic performance for CO$_2$ methanation.[13,14] Compared to Ni catalysts, Ni,Fe bimetallic catalysts reach a significantly improved catalytic activity.[15–19] For example, Grunwaldt and co-workers reported that a small addition of Fe to Ni/Al$_2$O$_3$ catalysts will increase activity and stability with an optimum ratio of Ni : Fe = 3 : 1.[20–22] They proposed that the redox cycle of iron species on Ni nanoparticles will promote the dissociation of CO$_2$ and further improve the activity.[23] Similarly, Huynh *et al.* reported a Ni : Fe ratio of 4 : 1 to be optimal.[24] It was also reported that CO$_2$ is hydrogenated

to HCOO* intermediates with a lower energy barrier. Meanwhile, other reports claim that the Ni-FeO$_x$ interfaces are more active for RWGS reaction due to its weak binding to CO* intermediates.[25]

On the other hand, CO$_2$ hydrogenation over supported Ni catalysts is highly structure-sensitive.[26–28] The size effect of Ni nanoparticles on CO adsorption has been proven to steer the selectivity of CO$_2$ hydrogenation, either to methane or to CO.[29,30] In addition, the support also plays as an important role for Ni catalysts in CO$_2$ methanation,[31–36] including its impact on the size and shape of the Ni nanoparticles (*i.e.* dispersion and morphology),[37] but also on CO$_2$ activation by the basicity and reducibility of the support.[38–40] Oxygen vacancies can be formed in reducible oxides during CO$_2$ hydrogenation, affecting the catalyst behavior. For example, in a series of Ni catalysts on different supports (Al$_2$O$_3$, ZrO$_2$, CeO$_2$), Ni supported on non-reducible Al$_2$O$_3$ shown the lowest CO$_2$ conversion.[31] Furthermore, strong metal-support interaction (SMSI) can affect the stability of CO$_2$ methanation, but also the selectivity.[41] Such effects typically are dynamic and depend on the reaction conditions and catalysts pre-treatments in a complicated manner. Monai *et al.* recently reported that such SMSI can generate interfacial sites on Ni/TiO$_2$ catalysts favoring carbon–carbon coupling and enhance the C$_{2+}$ species formation during CO$_2$ hydrogenation.[42]

So far, the effect of reducible supports on bimetallic Ni,Fe catalysts for CO$_2$ hydrogenation has not been studied to the same extent as the support effect on monometallic catalysts or the Fe promotion effect on unreducible supports.[43] In this

[a]*Institute of Inorganic Chemistry, Kiel University, Max-Eyth-Str. 2, 24118 Kiel, Germany. E-mail: schen@ac.uni-kiel.de, mbehrens@ac.uni-kiel.de*
[b]*Department of Inorganic Chemistry, Fritz-Haber-Institute of the Max-Planck-Society, Faradayweg 4-6, 14195 Berlin, Germany*
†Electronic supplementary information (ESI) available. See DOI: https://doi.org/10.1039/d4nr02025a

work, we first confirmed the intrinsic optimal Ni : Fe ratio for methanation on non-reducible, but basic MgO. Then, monometallic Ni and bimetallic Ni,Fe catalysts at this optimal ratio supported on MgO, ZrO_2 and CeO_2 have been compared to study if the promotional effect of Fe depends on the varying reducibility of the support by kinetic measurements, H_2-TPR, CO_2-TPD, and *in situ* DRIFTS measurements.

2. Experimental section

2.1. Catalyst preparation

The catalysts were prepared by the incipient wetness impregnation method. For the support of MgO, 1.25 mL of an aqueous solution containing $Fe(NO_3)_3 \cdot 9H_2O$ (99.5%, Grüssing GmbH) and $Ni(NO_3)_2 \cdot 6H_2O$ (99.9%, abcr GmbH) was added dropwise to 1 g of MgO (>99%, Alfa Aesar). The metal salt concentration was adjusted to reach a metal total (Ni and/or Fe) loading of 5 wt% on MgO. The wet powder was further stirred and then treated by ultrasonication for 15 min. After drying at 80 °C overnight, the collected pre-catalysts were directly reduced with $10\%H_2/N_2$ at 450 °C for 2 h prior to the catalytic tests. By changing the ratio between $Fe(NO_3)_3 \cdot 9H_2O$ and Ni $(NO_3)_2 \cdot 6H_2O$ in the aqueous solution, the molar ratio of Ni : Fe has been adjusted to 1 : 0, 5 : 1, 2 : 1, 1 : 1, 1 : 2, and 0 : 1. The reduced samples are labelled as Ni/MgO, Ni,Fe(83 : 17)/MgO, Ni,Fe(67 : 33)/MgO, Ni,Fe(50 : 50)/MgO, Ni,Fe(33 : 67)/MgO, and Fe/MgO respectively. The same procedure has been applied to the supports of ZrO_2 (99%, Alfa Aesar) and CeO_2 (99.5%, Alfa Aesar), but only monometallic Ni and a Ni : Fe ratio of 5 : 1 catalysts were selected, resulting in samples labelled as Ni/ZrO_2, Ni,Fe(83 : 17)/ZrO_2, Ni/CeO_2 and Ni,Fe(83 : 17)/CeO_2.

2.2. Catalysts characterization

Inductively coupled plasma optical emission spectroscopy (ICP-OES) was applied to analyze the elemental compositions of those catalysts supported on MgO and CeO_2. The pre-catalysts were dissolved in a mixture of nitric acid and hydrogen peroxide and measured on an Avio 200 ICP OES equipped with a S23 Autosampler (PerkinElmer). Due to the low solubility of ZrO_2, the metal compositions of these catalysts were determined in a scanning electron microscope by energy dispersive X-ray spectroscopy (SEM-EDX) using a Gemini Ultra55Plus (Zeiss).

The surface area was measured by N_2 physisorption using the Brunauer–Emmett–Teller (BET) method on a BELSORP MAX (Microtrac Retsch GmbH). The samples were pre-treated at 100 °C for 2 h in vacuum to remove adsorbed moisture and air. The isotherm was measured at −197 °C in liquid nitrogen.

Powder X-ray diffraction (PXRD) was used to study the crystal structure of the catalysts using Mo Kα radiation on a STADI P diffractometer (STOE). To avoid the re-oxidation of the reduced catalysts, the reduced samples were prepared in an Ar glovebox as sealed capillaries with 0.7 mm diameter and later measured in the Debye–Scherrer mode.

Hydrogen temperature programmed reduction (H_2-TPR) was performed on a BELCAT II catalyst analyzer (Microtrac Retsch GmbH) to study the reducibility of the catalysts. The measurements were conducted with 50 mg of the samples filled in a quartz glass fixed-bed micro-reactor. After pretreatment at 120 °C under on Ar flow for 1 h, the reactor was cooled down to 40 °C and then heated to 1000 °C at a rate of 6 °C min^{-1} in a 50 sccm of $10\%H_2/Ar$ flow. The reactor was later kept at 1000 °C for 15 min before cooling down and the H_2 consumption was measured with a thermal conductivity detector (TCD). The degree of the reduction (%) of the supported metal was estimated by the H_2 consumption assuming that full reduction corresponds to a state with all Ni and Fe being metallic, CuO was used to calibrate the H_2 consumption.

CO_2 temperature programmed desorption (CO_2-TPD) profiles were recorded with the home-built reaction setup equipped with TCDs on the inlet and outlet of the quartz tube reactor. Prior the measurement, all samples were heated to 450 °C with a rate of 5 °C min^{-1} in a 10 mL min^{-1} of 20% $H_2/$Ar flow. After an isothermal reduction at 450 °C for 2 h, samples were cooled down to 50 °C in a flow of He to remove the residual gases from the reduction. CO_2 adsorption was carried out at 50 °C for 2 h with a flow rate of 10 mL min^{-1}. Then a 10 mL min^{-1} of He was introduced to remove physically adsorbed CO_2 before the desorption. CO_2-TPD curve was drawn at the temperature range from 50 to 600 °C with the heating rate of 10 °C min^{-1}. The number of surface basic sites was calculated using the integration of the calibrated CO_2 peak below the curve. The raw data were smoothed first and then fitted (Fig. S3, ESI†) into three Gaussian peaks at different temperature ranges representing the weak, medium and strong basic sites.

Transmission Electron Microscopy (TEM) was employed to evaluate the nanoparticle size of the freshly reduced samples. TEM images were taken in the bright field mode on a Tecnai F30 G2 S-TWIN (Thermo Fisher Scientific) equipped with a field emission gun (FEG) using an acceleration voltage of 300 kV and a spherical aberration coefficient of 1.2 mm. Due to the low metal loading and small nanoparticle size, the brightness and contrast of TEM images were adjusted to clearly identify metal particles.

Diffuse Reflectance Infrared Fourier Transform Spectroscopy (DRIFTS) measurements were performed on the reduced catalyst following the adsorption and desorption of CO used as a probe molecule. The samples were heated up to 450 °C with 5 °C min^{-1} in an 80 mL min^{-1} flow of $10\%H_2/$He and then an isothermal reduction was performed for 2 h. Afterwards, the reduced catalysts were purged in pure He for 30 min and then cooled down to 10 °C. The analysis was performed under 80 mL min^{-1} of 0.5% CO/He mixture flow for 40 minutes during adsorption and pure He flow for 40 minutes during desorption. The spectra were collected by a iS50 FTIR spectrometer (Thermo Fisher Scientific) equipped with a high-temperature reaction chamber (Praying Mantis, Harrick) coupled with a dome mounting ZnSe windows. All

measurements were collected by the OMNIC software *via* an automatic series collection using a Gram-Schmidt method. The temperature was controlled by Harrick ATC and a Huber Ministat 125 chiller. No compensation of H_2O and CO_2 signal was used.

2.3. Kinetic measurements

Catalytic tests were performed in a U-shaped micro-reactor where the catalyst bed was fixed by quartz wool plugs. A thermocouple was inserted directly into the catalyst bed to measure the temperature. After isothermal reduction at 450 °C for 2 h, the reactor was cooled down to 350 °C and 50 sccm of a reaction gas mixture was injected into the reactor to start the CO_2 hydrogenation test at atmospheric pressure, consisting of 9.6% CO_2/N_2, 38.4% H_2 and balanced N_2. The inlet gas flow was controlled by mass flow controllers (Bronkhorst) and the gas composition at the exhaust was evaluated by a micro-GC (INFICON). In a typical catalytic test, 30 mg of MgO-supported catalysts were used while 10 and 3 mg of the ZrO_2 and CeO_2-supported catalysts were sufficient to reach a similar CO_2 conversion of less than 25% to ensure the measured selectivity for methanation can be compared at similar conversion levels. The catalyst sieve fraction of 200–300 μm was diluted with 350–460 μm SiC (Thermal Scientific) to give a total weight of 200 mg to avoid heat and mass transfer issues.

The activation energies (E_a) of selected catalysts were measured at temperatures ranging from 315 to 355 °C and reaction orders for H_2 and CO_2 were tested in the same reactor at 350 °C by changing the respective partial pressures. All the kinetic measurements were conducted under low CO_2 conversion of less than 25%.

As shown in eqn (1), the reaction rates of CO_2 hydrogenation were defined as the CH_4 production rate (r_{CH_4}) for methanation and the CO production rate (r_{CO}) for the RWGS normalized to the weight of active metals. The conversion of CO_2 and the selectivity for CH_4/CO were calculated as eqn (2) and (3).

$$r_{CH_4/CO} = \frac{\text{Flow rate} \times \text{conc.}_{CH_4/CO}}{g_{cat.} \times \text{wt\%}} \quad (1)$$

$$\text{Conv.}_{CH_4/CO} = 1 - \frac{\text{conc.}_{CO_2,out}}{\text{conc.}_{CO_2,in}} \quad (2)$$

$$\text{Selec.}_{CH_4/CO} = \frac{\text{conc.}_{CH_4/CO}}{\text{conc.}_{CH_4/CO} + \text{conc.}_{CO/CH_4}} \quad (3)$$

3. Results

The metal loading of the as-synthesized samples was checked by ICP-OES and SEM-EDX, which confirmed the total metal loading are approximately 5 wt% for all the samples (Tables S1 and 2, ESI†). For the bimetallic catalysts, also the measured Ni : Fe ratios are in reasonable agreements with the nominal values (Tables S1 and 2, ESI†). The BET surface areas of the commercial supports are approximately 15 (MgO), 26 (ZrO_2), and 64 (CeO_2) m^2 g^{-1} (Table S3, ESI†). The reducibility of the

Ni,(Fe)/MgO catalysts was studied by H_2-TPR (Fig. 1a). With increasing Fe content, the reduction peaks gradually shift to higher temperatures. Such trend is consistent with previous reports and can be explained by the less noble nature of iron compared to nickel.[44,45] A single TPR peak was observed for the reduction into the metallic state indicating presence of uniform metal species.[46,47] Only a weak shoulder is observed at the lower temperature side of the TPR profile (around 400 °C) with increasing Fe content, which can be assigned to the intermediate reduction of Fe^{3+} to Fe^{2+}.[47–49] There is no significant reduction at temperatures higher than 500 °C for all the MgO-supported catalysts confirming the unreducible nature of the support at these conditions. Thus, an isothermal reduction at 450 °C for 2 h was chosen to reach a full reduction of both Ni and Fe. The XRD patterns of the freshly reduced samples are shown in Fig. 1b. The major crystalline phase in all catalysts is MgO while there are no obvious reflections of Ni or Fe metal detected, which can be explained with the low loading of active metal and the small crystallite size.

The catalytic performance of the reduced Ni,Fe/MgO catalysts for CO_2 hydrogenation was evaluated at 350 °C for 16 h after the above-described reduction step. Both of the monometallic Ni and Fe catalysts showed stable activity in methanation and RWGS (Fig. 2) and, as expected, Ni had a higher activity and selectivity to methane. Note that it was reported that the addition of low amounts of Fe to Ni catalysts can prohibit the deactivation of monometallic Ni catalyst,[22,50] but no such deactivation was present for the MgO-supported monometallic Ni in our experiment. However, the bimetallic Ni,Fe catalysts showed high CO_2 conversions at the beginning, but suffer from gradual deactivation over 16 h time on stream (TOS). In this process, methanation deactivated stronger than RWGS leading to a decrease of CH_4 selectivity (Fig. 2b–d). Sintering and carbon deposition are the most probable reasons for such initial deactivation.[51–53] Under methanation reaction conditions, it has been reported that small Ni nanoparticles may coalesce to form bigger particles, followed by the Ostwald ripening.[54,55] The particle size growth can also be associated to the formation of metal carbonyls due to the enhanced mobility of $Ni(CO)_x$ species.[55–57] The particle size increase will result in the loss of surface area and active sites, eventually resulting in the deactivation of catalysts. After 16 h TOS, both the methanation and RWGS rates have approached to a steady-state for each catalyst, revealing a volcano-shaped trend with the Fe loading (Fig. 3). The optimal Ni : Fe ratio for the CO_2 hydrogenation was identified as 5 : 1, *i.e.* Ni,Fe(83 : 17)/MgO, with the highest activity in both methanation (0.035 mmol$_{CH_4}$ g$_{metal}^{-1}$ s^{-1}) and RWGS (0.302 mmol$_{CO}$ g$_{metal}^{-1}$ s^{-1}). It was proposed that iron oxide species can be formed from the oxidation of iron by CO_2 and H_2O in the gas stream. These can be dispersed on the Ni particles, and the redox cycle of oxidized Fe species can promote the CO_2 hydrogenation.[20–23] A similar dynamic promotion effect in Co,Fe bimetallic catalysts in CO_2 hydrogenation was interpreted as a result of alloy formation after reduction of bimetallic catalysts.[58] In both scenarios, a too strong increase in Fe loading will cause either blocking or
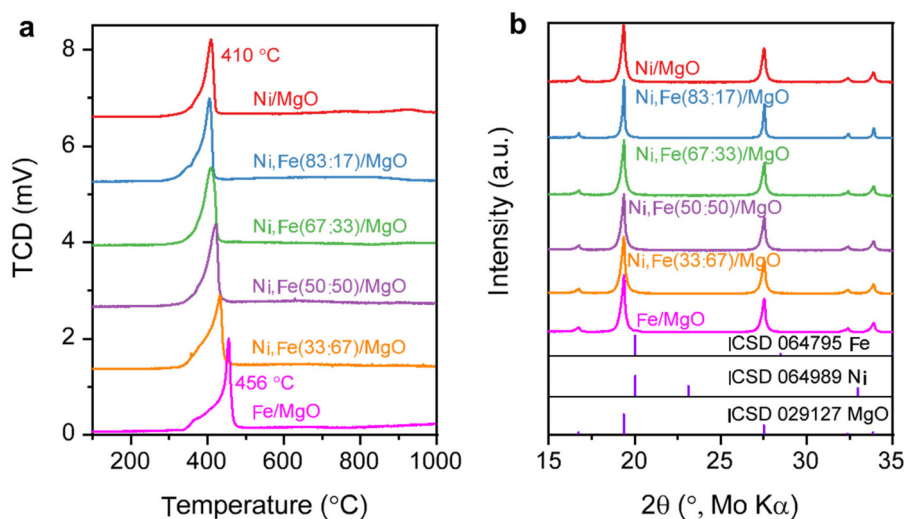
Fig. 1 (a) H$_2$-TPR profile for Ni,Fe monometallic and bimetallic catalysts supported on MgO and (b) their PXRD patterns after isothermal reduction of 450 °C.
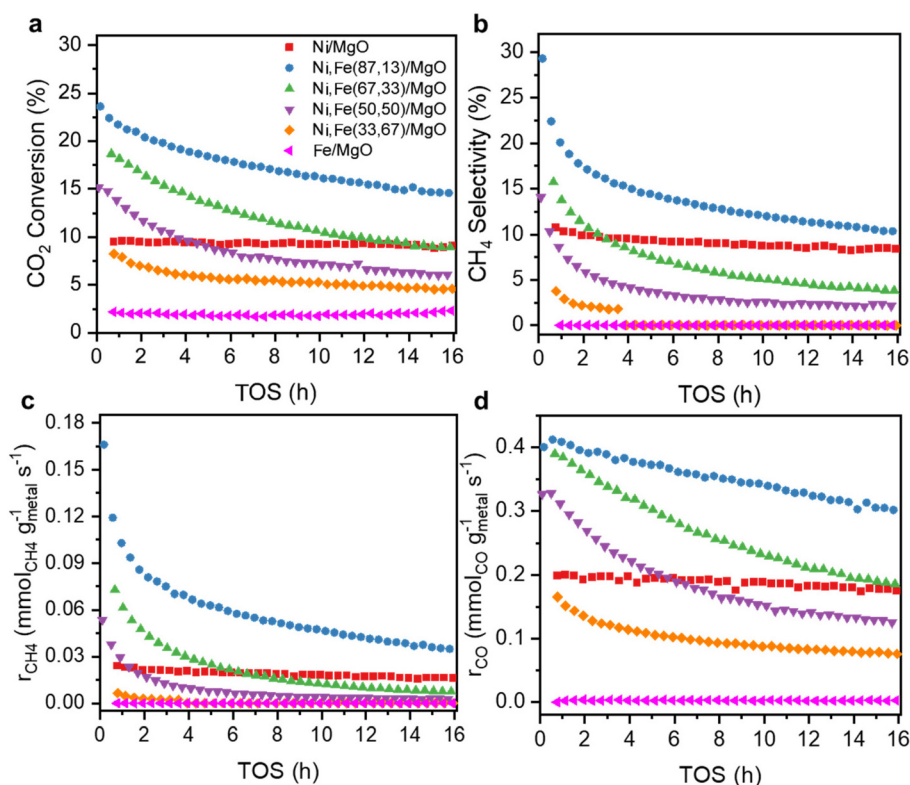

Fig. 2 (a) CO$_2$ conversion, (b) selectivity towards CH$_4$, (c) methanation rate and (d) RWGS rate as a function of TOS for MgO-supported catalysts with various Ni : Fe ratios at 350 °C.

substitution of active Ni sites at the surface, which explains the decreased activity with higher Fe loading, which is not uncommon for promoter species. Besides, our Ni,Fe bimetallic catalysts also suffer from deactivation, which might be associated with the gradual and dynamic formation of such oxidized Fe "islands".

The Ni,Fe(83 : 17)/MgO catalyst reached the highest reaction rate of both methanation and RWGS reactions with the highest CH$_4$ selectivity in this series of catalysts (~10.2%) (Fig. 2b–d). This ratio of 5 : 1 for Ni : Fe has been employed in the study of the other two supports, *i.e.* ZrO$_2$ and CeO$_2$, to investigate the support effect on the Ni,Fe bimetallic catalysts for CO$_2$ hydrogenation.
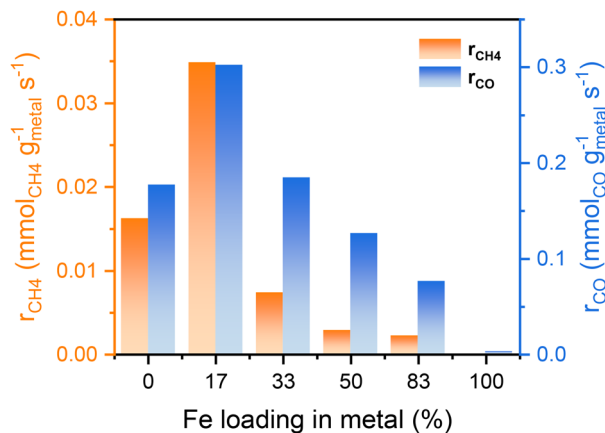
Fig. 3 Reaction rates of both methanation and RWGS after 16 h test for different Fe loadings in Ni,(Fe)/MgO catalysts.

The reducibility of these two series catalysts was studied first. The H_2-TPR profiles of ZrO_2 and CeO_2 supported catalysts exhibit two reduction peaks below 400 °C, which could result from weakly and strongly bound Ni^{2+} and Fe^{3+} species[59,60] (Fig. 4a), indicating the reduction of the metal completes before 450 °C. Besides, the reduction degree (%) of the supported metal estimated by the H_2 consumption assuming that all Ni and Fe can be fully reduced were compared among these mono- and bimetallic supported catalysts, following the order $CeO_2 \rightarrow ZrO_2 \rightarrow$ MgO-supported catalysts (Fig. 4c). The higher reduction degree of CeO_2- and ZrO_2-supported catalysts agree with the reducibility of these oxides. For the CeO_2-supported catalysts, reduction degree even higher than 100% clearly indicate that support species have been reduced together with the metal oxide species at low temperature (<300 °C), agreeing well with the previous report of co-reduction of highly dispersed metal and support-CeO_2,[61–63] which was explained by metal-

support interaction (MSI) and/or hydrogen spillover effects.[64–68]

The XRD patterns of these reduced samples show broad reflections for Ni and Fe at around 20° 2θ, which might be due to the small metal particle size or low metal loading (Fig. 4b). The broad XRD peak profiles agree well with the TEM images showing that most metal nanoparticles have a size around 5–10 nm (Fig. 5). Similar nanoparticle sizes were found for all six catalysts, which indicates that the comparison here is not strongly affected by possible size effects on CO_2 hydrogenation.[69]

All supported Ni and Ni,Fe(83 : 17) catalysts were studied in the CO_2 hydrogenation reaction at 350 °C for 16 h. The CO_2 conversion is similar for monometallic Ni and bimetallic Ni,Fe (83 : 17) catalysts on both supports ZrO_2 and CeO_2, suggesting in contrast to MgO-supported catalysts, no clear promotion effect of Fe on the CO_2 conversion for these reducible supports (Fig. S2, ESI†). Monometallic Ni even showed a higher CO_2 methanation rate than bimetallic Ni,Fe(83 : 17) if supported on ZrO_2 or CeO_2 (Fig. 6) showing a negative effect of Fe addition on the methane selectivity. Actually, Winter *et al.* already found that the introduction of Fe to Ni catalysts supported on CeO_2 will increase the selectivity towards RWGS.[70] They proposed that the formation of oxidized Fe will weaken the CO binding strength, resulting in desorption. Since the adsorbed CO is one of the potential intermediates for methanation, this can explain the lower selectivity to CH_4 in favor or RWGS.[71] However, this is very different to MgO-supported catalysts where the addition of Fe enhances both CO_2 conversion and methane selectivity, though on a lower level of around 10%. The absolute selectivity to methane for Ni/CeO_2 and Ni/ZrO_2 were much higher than on MgO and reached 82.3% and even 94.4%, indicating that the methanation reaction is greatly promoted by the reducible nature of the oxide support with a much stronger effect than the presence or absence of Fe.
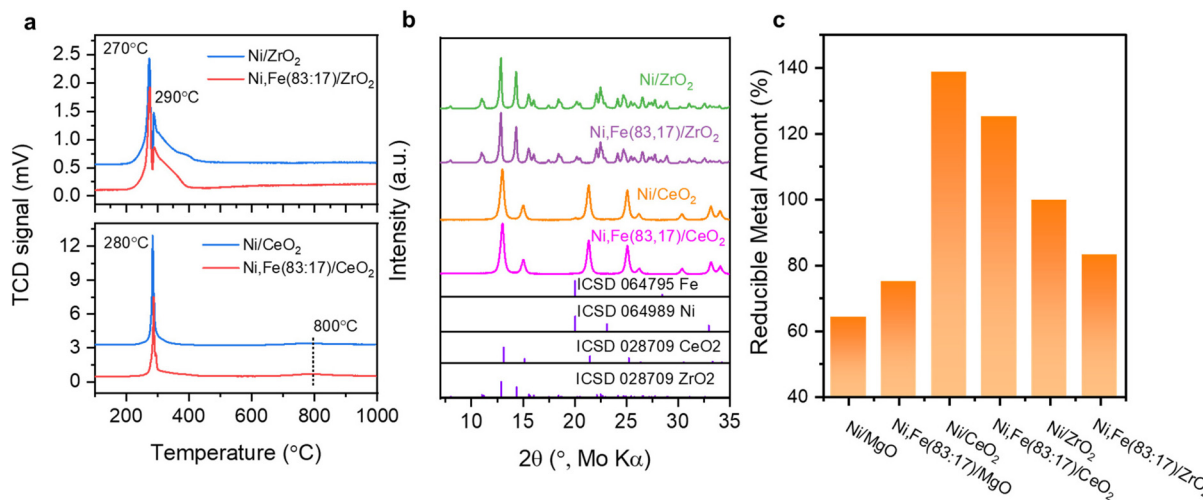

Fig. 4 (a) H_2-TPR profile for Ni monometallic and Ni,Fe bimetallic catalysts supported on ZrO_2, CeO_2; (b) the PXRD patterns of the samples reduced isothermally at 450 °C and (c) the estimated degree of reduction, where valued beyond 100% refer to co-reduction of support species.
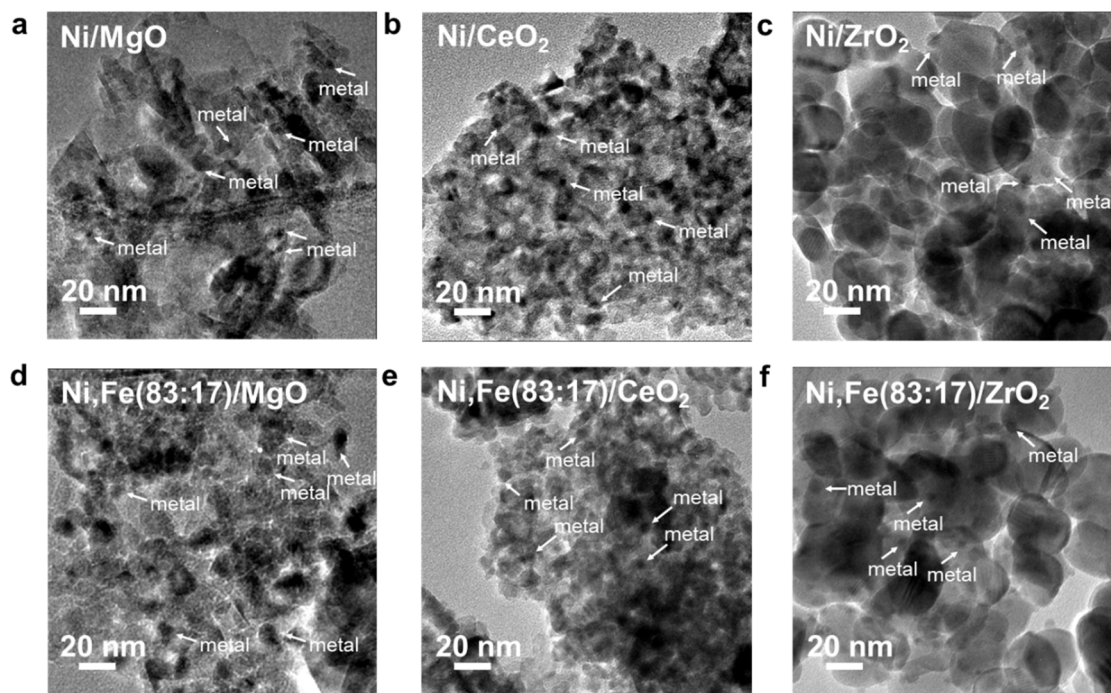
Fig. 5 TEM images for Ni–Fe monometallic and bimetallic catalysts supported on (a) & (d) MgO, (b) & (e) ZrO$_2$ and (c) & (f) CeO$_2$.
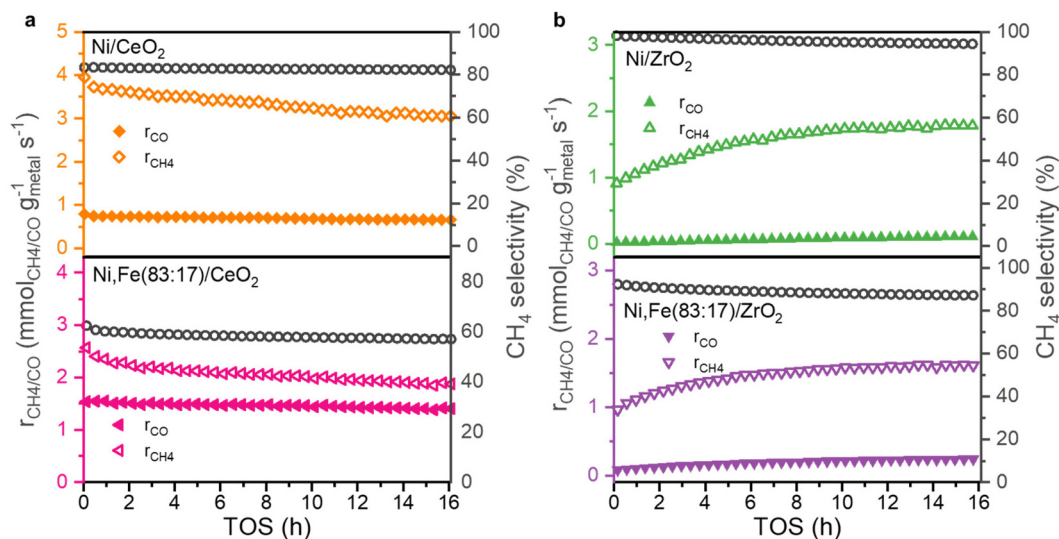

Fig. 6 Methanation and RWGS rates and selectivity towards CH$_4$ as a function of TOS for (a) CeO$_2$ and (b) ZrO$_2$-supported monometallic and bimetallic catalysts for 16 h TOS at 350 °C.

While the selectivity remains quite stable during the 16 hours TOS (Fig. 6), the conversions show an interesting trend (Fig. S2, ESI†). The CeO$_2$-supported catalysts show a slight deactivation, which is much less pronounced compared to Ni,Fe(83 : 17)/MgO, but for the ZrO$_2$ supports, a clear activation phase in both of methanation and RWGS reactions was observed. A similar behavior was found before in Ru/ZrO$_2$ in CO$_x$ methanation,[39,72] which was explained by the slow

reduction of ZrO$_2$ leading to increasing metal-support interaction during the hydrogenation reaction.

The reaction pathways on Ni/ZrO$_2$ and Ni/CeO$_2$ catalysts discussed in the literature indeed assume a strong involvement of the support. CO$_2$ is first adsorbed on a hydroxyl group of the ZrO$_2$/CeO$_2$ support. There, it can be hydrogenated to formate by dissociated hydrogen from metallic Ni under desorption of H$_2$O.[73–77] The formate intermediate can either decompose and

then transfer onto the surface of the metallic Ni nanoparticle or directly be converted on the ZrO_2/CeO_2 surface to CH_4 by combing with more dissociated hydrogen spilled over from Ni.[73,75–77] Both reaction pathways require a strong participation of ZrO_2/CeO_2 in the CO_2 activation steps. The latter pathway even avoids adsorption of any carbon- or oxygen-bound intermediates on the surface of Ni, which could help to keep the metallic Ni particles free from deactivating species. Contrarily, for the catalysts supported on MgO, CO_2 and its CO* or HCOO* intermediates may absorb mainly on the Ni surface, which increases the probability of strong deactivation by oxidation or coking.[7]

Comparing the steady-state activity (after 16 h TOS) among these Ni and Ni,Fe catalysts supported on three different oxides, the CeO_2 supported catalysts show the highest activity. Ni/CeO_2 has the highest methanation rate of 3.0 $mmol_{CH_4}$
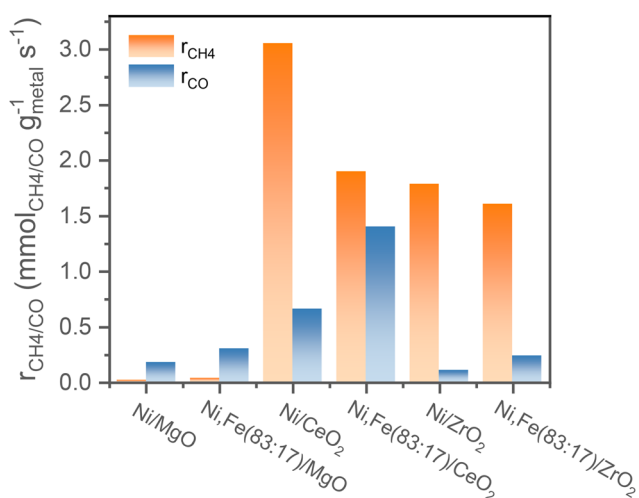

Fig. 7 Comparison of the reaction rates of the different supported mono- or bimetallic catalysts for both methanation and RWGS after 16 h TOS.

g_{metal}^{-1} s^{-1} and $Ni,Fe(83:17)/CeO_2$ has the highest RWGS rate of 1.3 $mmol_{CO}$ g_{metal}^{-1} s^{-1} (Fig. 7). The steady-state activity of the methanation reaction followed the order of MgO-supported < ZrO_2-supported < CeO_2-supported, which agrees well with the reducibility order: MgO < ZrO_2 < CeO_2 and underlines to role of a SMSI or electronic metal-support interaction (EMSI) effect.[18,33,39,78] The basicity of the Ni-based monometallic catalysts and their bare support were investigated through CO_2-TPD experiments (Fig. 8 and Table 1). CO_2-TPD profiles revealed three Gaussian peaks representing the weak (100–170 °C), medium (222–302 °C), and strong (396–501 °C) basic sites. The low-temperature peak corresponds to the CO_2 desorption from weak Brønsted sites.[79–82] The medium-temperature peak originates from bidentate carbonates on metal–oxygen pairs such as Mg–O.[79–82] The high-temperature peak is correlated to the desorption of unidentate carbonates on low-coordination O^{2-} anions.[79–83] Based on the quantitative analysis of CO_2-TPD profiles, Ni/CeO_2 catalysts have the highest content of weak basic sites (29 $μmol_{CO_2}$ g_{cat}^{-1}) among these three supported Ni catalysts, which indicates that the CeO_2 support can facilitate the CO_2 adsorption, contributing to its high activity.[84–86] Furthermore, compared to the bare support, our results suggest that CeO_2-supported catalysts have a higher total density of basic sites (85 $μmol_{CO_2}$ g_{cat}^{-1} for Ni/CeO_2 *vs.* 54 $μmol_{CO_2}$ g_{cat}^{-1} for CeO_2), whereas a lower total basic sites

Table 1 Calculated basic site density based on the results from CO_2-TPD of the bare supports and the reduced catalysts

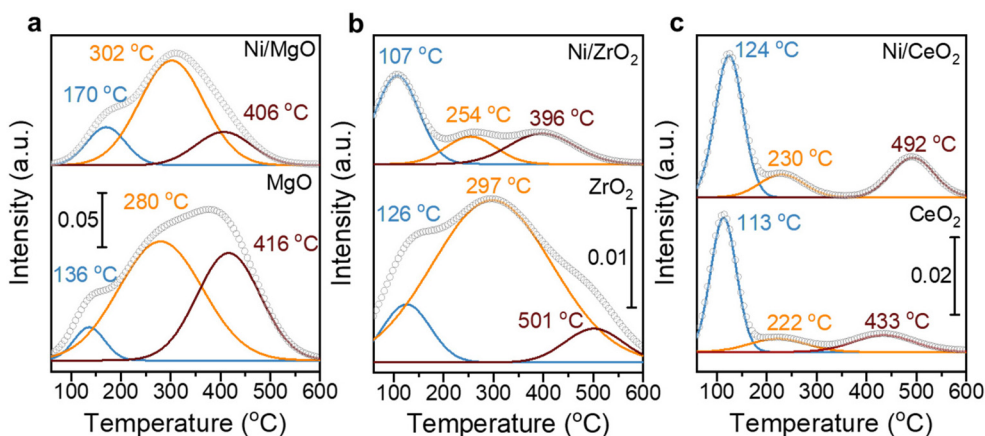|	Weak [$μmol$ g^{-1}]	Medium [$μmol$ g^{-1}]	Strong [$μmol$ g^{-1}]	Total [$μmol$ g^{-1}]
MgO	15	87	65	167
Ni/MgO	17	72	21	111
ZrO_2	11	52	22	85
Ni/ZrO_2	12	7	7	26
CeO_2	27	8	19	54
Ni/CeO_2	29	19	37	85

Fig. 8 CO_2-TPD profiles at 10 °C min^{-1} for (a) MgO, (b) ZrO_2, (c) CeO_2 supports, and their corresponding Ni loaded catalysts where grey dots represent the smoothed raw profiles and the solid color lines indicate the fitting results for week, medium and strong basic sites at different temperatures.

density was observed for the MgO-supported (111 μmol_{CO_2} g_{cat}^{-1} for Ni/MgO vs. 167 μmol_{CO_2} g_{cat}^{-1} for MgO) and ZrO_2-supported (26 μmol_{CO_2} g_{cat}^{-1} for Ni/ZrO_2 vs. 85 μmol_{CO_2} g_{cat}^{-1} for ZrO_2) samples. Notably, experimental results have revealed that MgO and its catalysts release significantly more CO_2 during the TPD experiments. This increased CO_2 release is likely related to the presence of bulk carbonates formed during CO_2 adsorption[87,88] and is not necessarily indicative of surface basicity. Nevertheless, these results clearly demonstrate that the SMSI in Ni/CeO_2 catalyst results in interfacial sites more favorable for CO_2 activation/conversion. As Ni/CeO_2 contains a higher density of basic sites than the bare support CeO_2, and given than the density of basic sites can be correlated to the oxygen vacancy density, this is consistent with the results of the H_2-TPR analysis.[89,90]

Further kinetic experiments were conducted for Ni and Ni, Fe catalysts to determine the apparent activation energy (E_a) and reaction order of CO_2 and H_2 with respect to methanation and RWGS for a deeper investigation of the support effect. From the Arrhenius plot shown (Fig. 9a–c), the apparent activation energy E_a for MgO and CeO_2 supported catalysts are very similar between 71 and 79 kJ mol^{-1} in both methanation and RWGS reactions. However, the intercepts in the Arrhenius plot for the MgO-supported catalysts are much lower than for the CeO_2-supported catalysts, suggesting more actives sites from the latter catalysts. This interpretation agrees with the previous hypothesis that the metal-support interaction provides additional abundant active sites at the ceria-metal interfaces. Besides, the high reducibility of CeO_2 results into more oxygen vacancies introducing the so-called electronic metal-support-interaction (EMSI) effect, which can activate CO_2 at lower temperatures.[18] For ZrO_2-supported catalysts, the Arrhenius plots suggest a different activation energy compared to MgO- and CeO_2-supported catalysts. Here, the E_a of methanation is 94.4 kJ mol^{-1}, which is almost half of that of RWGS (196.6 kJ mol^{-1}), implying that the relative barrier energy for RWGS is very high

on this type of catalyst. The big difference in activation energy for these two reactions on Ni/ZrO_2 can account for the highest methane selectivity for ZrO_2-supported catalysts.

The reaction orders of CO_2 and H_2 for monometallic Ni and bimetallic Ni,Fe catalysts were studied for understanding of the limiting factors of reactants activation (Fig. 10 and 11). For the three monometallic Ni catalysts, an increasing in CO_2 partial pressure affected the RWGS more than methanation, suggesting that the RWGS is limited by the activation of CO_2, especially for Ni/CeO_2 with the highest CO_2 reaction order of 1.08 in RWGS (Fig. 10a–c). At the same time, the H_2 partial pressure variation affected the methanation rate stronger and positively showing that the methanation is rather limited by the activation of H_2. The RWGS was even affected negatively by an increase in the H_2 partial pressure for the two catalysts on the reducible supports, CeO_2 and ZrO_2, especially for ZrO_2-supported catalysts with a value of -0.86 (Fig. 10d–f). The high selectivity towards CH_4 for the ZrO_2-supported catalysts can therefore also be explained by the hydrogen-rich condition ($H_2 : CO_2 = 4 : 1$), which also agrees well with the previous results of activation energy. In addition, as the calculated reduction degree of CeO_2 supported catalysts exceeds 100%, indicating that not only Ni and Fe were activated to the metallic state, but CeO_2 was also partially reduced to CeO_{2-x}, forming surface oxygen vacancies.[91,92] The oxygen vacancies donate electrons which could participate in the adsorption and activation of CO_2, explaining the reason that the CeO_2 supported catalysts with relatively rich oxygen vacancies have a higher CO_2 reaction order in both methanation and RWGS (Fig. 10). Furthermore, the H_2-spillover effect is supported by the H_2-TPR result where the reduction of surface CeO_2 occurs at around 280 °C, significantly lower than the surface reduction temperature of pure CeO_2, which is normally around 450 °C.[62,93,94] This indicates that the dissociated H migrate from the metal to the metal-support interface and can hydrogenate the activated CO_2.
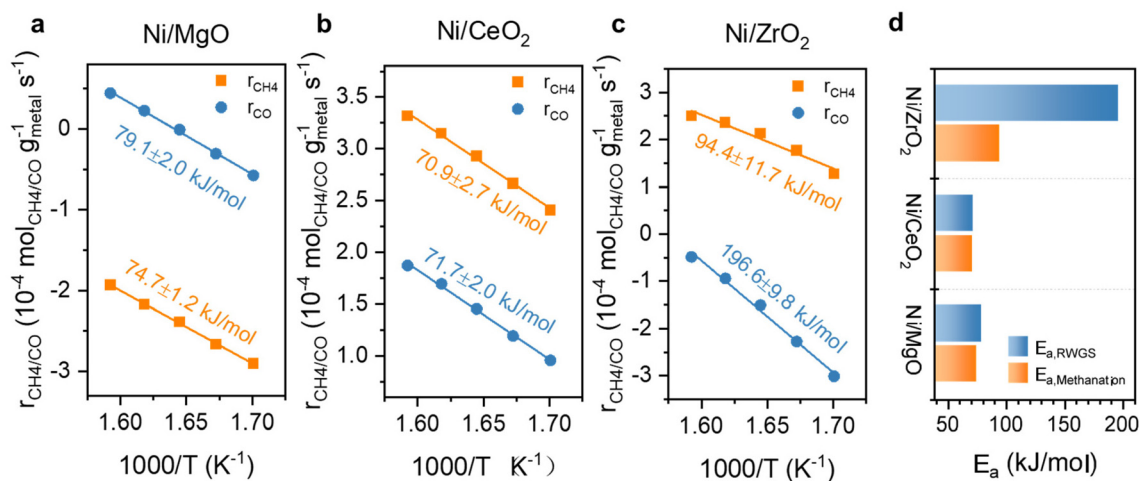

Fig. 9 Arrhenius plots with calculated E_a for Ni catalysts supported on (a) MgO, (b) CeO_2, (c) ZrO_2 and (d) comparison of their E_as for RWGS and methanation.
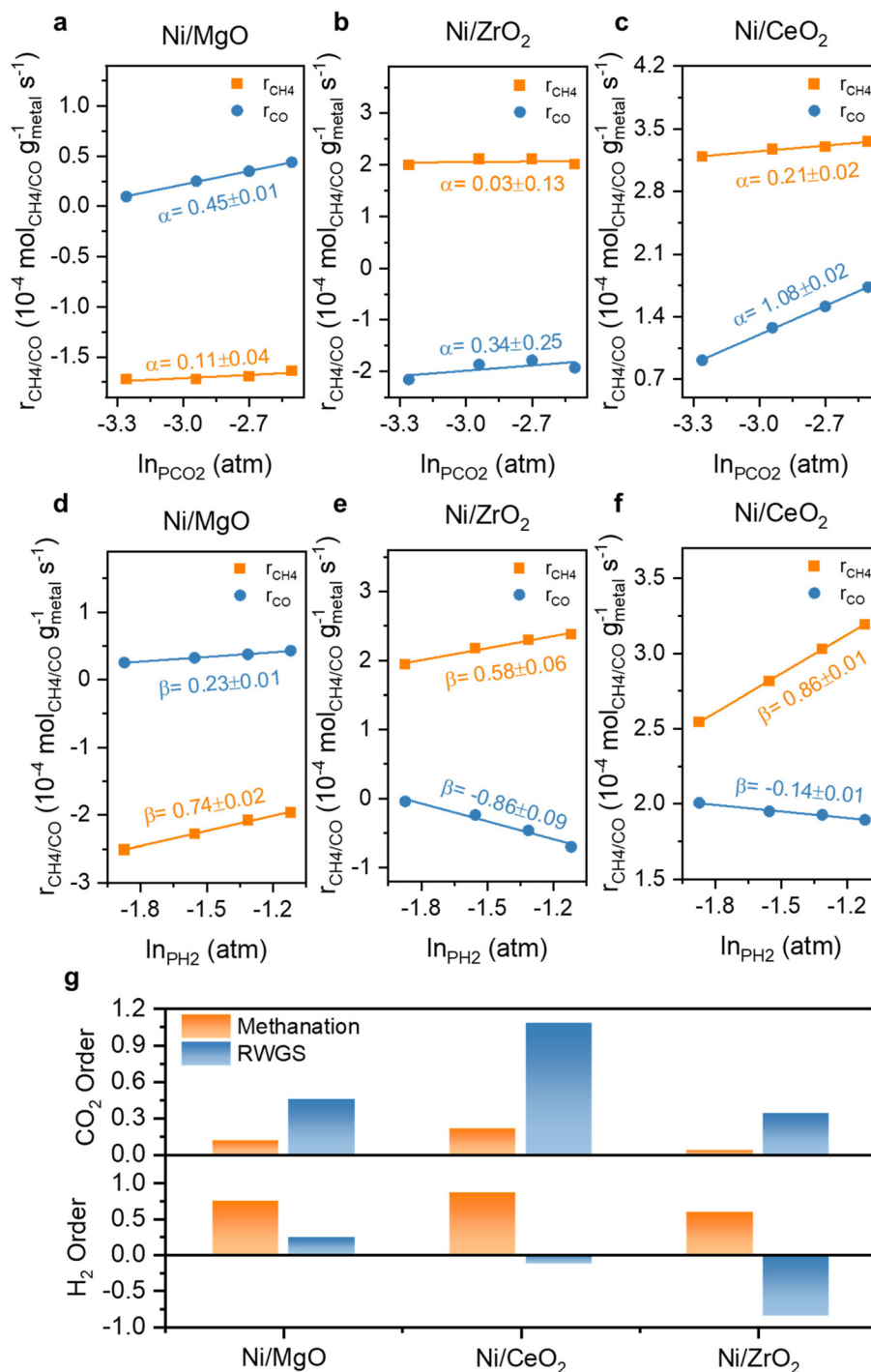
Fig. 10 The reaction order of CO_2 (α) and H_2 (β) at 350 °C for Ni monometallic catalysts supported on (a) & (d) MgO, (b) & (e) ZrO_2 and (c) & (f) CeO_2 and (g) their comparison.

The reaction orders of CO_2 and H_2 for the bimetallic Ni,Fe catalysts are shown in Fig. 11. Compared to the monometallic catalysts, there was a more significant increase in both reaction orders of CO_2 and H_2 for methanation compared to RWGS reaction on the MgO-supported catalyst, corresponding to the higher methanation selectivity on the bimetallic catalysts (Fig. 2). For the ZrO_2-supported catalyst Ni,Fe(83 : 17)/ZrO_2, the H_2 reaction order

of $−0.21$ in RWGS was still negative but has increased strongly from $−0.86$ observed in Ni/ZrO_2. This less negative H_2 reaction order showed that the H_2-inhibition of RWGS was mitigated compared to the monometallic Ni catalyst, consistent with a lower RWGS selectivity on this bimetallic catalyst (Fig. 6b). Notably, introducing Fe to Ni/CeO_2 minorly modified the reaction order of CO_2 or H_2 in both methanation and RWGS.
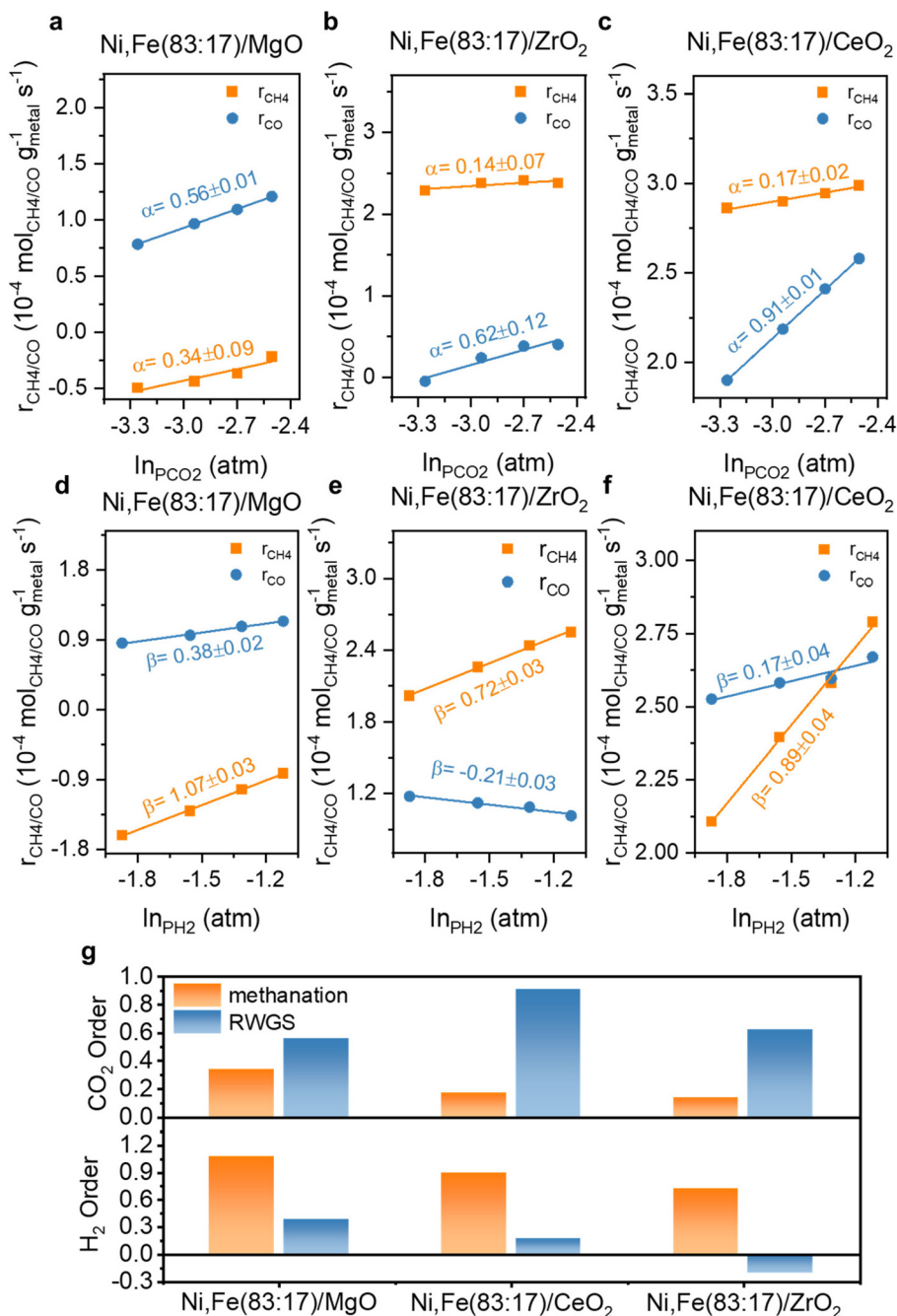
Fig. 11 The reaction order of CO_2 (α) and H_2 (β) at 350 °C for Ni,Fe bimetallic catalysts supported on (a) & (d) MgO, (b) & (e) ZrO_2 and (c) & (f) CeO_2 and (g) their comparison.

Additionally, *in situ* DRIFTS combined with CO as a probe were performed on the Ni monometallic catalysts to study the impact of the support on the surface properties of Ni. The formed surface species during CO adsorption can be divided in two main regions: one with spectral features above 1800 cm^{-1} and the other with features below 1800 cm^{-1}. For Ni/MgO, the spectra region above 1800 cm^{-1} is characterized by adsorbed CO (CO_{ad}) species *i.e.* the metal carbonyl, in particular the linear Ni^0-CO species (2056 and 2029 cm^{-1}) and the

bridged $(Ni^0)_x$-CO species (1945 and 1919 cm^{-1}).[95,96] At features below 1800 cm^{-1}, several bands can be identified as carbonate, bicarbonate, and formate species.[95,97–99] The intensity of carbonaceous/carbonate-like species and CO_{ad} species increased as a function of the CO adsorption time (Fig. 12a). In the desorption period (Fig. S4, ESI†), CO_{ad} species gradually diminished and left a bit amount of CO_{ad} adsorbed on the Ni surface while carbonate, bicarbonate, formate species region remained after 40 min of desorption.
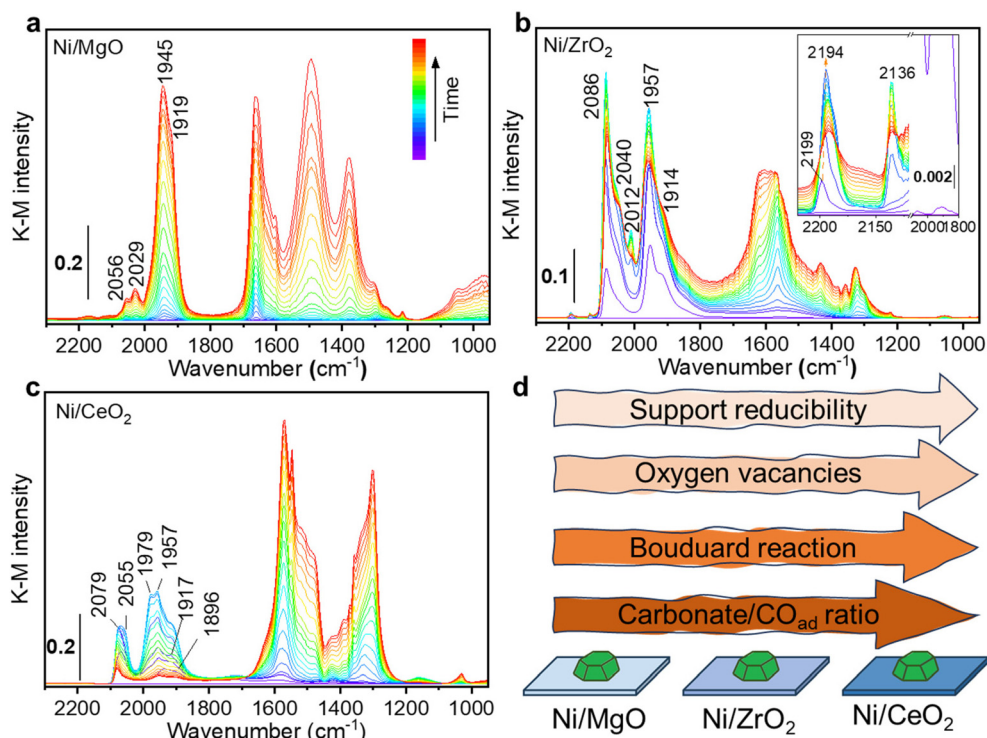
Fig. 12 *In situ* DRIFTS spectra of (a) Ni/MgO, (b) Ni/ZrO$_2$ and (c) Ni/CeO$_2$ catalysts collected during CO adsorption, inset images in (b) representing the zoom-in spectra at features above 2100 cm^{-1}. Illustration (d) of the structural properties changes in three different supported Ni Catalysts.

For Ni/ZrO$_2$, CO adsorption resulted in the formation of a very intense peak at 2086 cm^{-1}, with a shoulder at 2040 cm^{-1}, which was ascribed to linear Ni^0-CO (Fig. 12b). At higher frequency, two tiny peaks were identified and ascribed to linear Ni^{2+}-CO (2199–2194 cm^{-1}) and Ni$^+$-CO (2136 cm^{-1}).[96] Besides, the two bands at 1957 and 1914 cm^{-1} were ascribed to bridged (Ni^0)$_x$-CO species. In the lower frequency region below 1800 cm^{-1}, several bands were observed and identified as carbonate and bicarbonate species, similar to Ni/MgO. During the CO adsorption, the intensity of all CO$_{ad}$ bands increased to a maximum after about 6 minutes and then started to decrease. Meanwhile, a continuous increase in the range of the carbonaceous/carbonate-like species bands was observed. This change of the intensity was interpreted as Boudouard reaction (2 CO → CO$_2$ + C) on the active sites of Ni.[100]

The disproportionation of CO to carbon would result in the partial encapsulation of some Ni sites and a lower intensity for CO$_{ad}$ species. Meanwhile, the produced CO$_2$ can be adsorbed and formed the carbonate species on the adjacent ZrO$_2$. Note that one cannot exclude a direct CO adsorption contributing to the formation of carbonaceous/carbonate-like species as described for Ni/MgO. In the desorption process, except for the bands of ionic Ni^{n+}-CO species, almost all the bands are stable and still present during purging in He (Fig. S5, ESI†). Only the linear Ni^0-CO species lost more than half of its intensity, suggesting the presence of less stable Ni^0-CO species.

Regarding the Ni/CeO$_2$ catalyst, CO adsorption led to the formation of the similar species observed for Ni/MgO: linear Ni^0-CO (2079 and 2055 cm^{-1}) and bridged (Ni^0)$_x$-CO (1979, 1957, 1917 and 1896 cm^{-1}) species.[96] Various carbonate-like species bands were observed and were ascribed to the CeO$_2$ support in the frequency region lower than 1800 cm^{-1}. In the CO adsorption process, similarly to the Ni/ZrO$_2$ sample, a change of the CO$_{ad}$ species intensity was observed. This behaviour becomes even more remarkable on Ni/CeO$_2$ than Ni/ZrO$_2$, with a major intensity reduction that drastically reduces the intensity of all CO$_{ad}$ species. Such behaviour could be related to the stronger reducibility of CeO$_2$ than ZrO$_2$, which was also proved by the H$_2$-TPR results (Fig. 4). Compared to Ni/ZrO$_2$, more oxygen vacancies of Ni/CeO$_2$ formed during reduction pre-treatment (proved by H$_2$-TPR) drove a more pronounced charge transfer between Ni and reduced CeO$_2$ (EMSI effect), resulting in a higher electron density on Ni sites in Ni/CeO$_2$ catalyst, which leads to a more active CO disproportionation (Fig. 12d). Such concept that charge transfer from oxygen vacancies to adjacent metal sites through EMSI effect has been also demonstrated on Ru/ZrO$_2$ catalysts both in experimental and theoretical aspects.[72] Moreover, the formation of carbon layer on the top of Ni^0 sites during disproportionation would inhibit the further adsorption of CO molecules. Such hypothesis is consistent with the observation that the intensity of CO$_{ad}$ species were much lower than the carbonate bands on Ni/CeO$_2$ catalyst (Fig. 12c). During the desorption process, almost all CO$_{ad}$ species disappeared (Fig. S6, ESI†), suggesting a very labile nature of these species and influenced by a stronger electron density transferred from the reduced CeO$_2$

support. At the same time, the carbonaceous/carbonate-like species slightly increased in intensity, indicating that some CO molecules could have been re-adsorbed to form carbonaceous/carbonate-like species after being desorbed from Ni^0 sites.

4. Discussion

The support effect on the Ni,Fe bimetallic catalysts as well as Ni monometallic catalysts in CO_2 hydrogenation (methanation and RWGS) studied here can be summarized and interpreted as follows:

1. On a series of Ni-based (Ni,Fe) catalysts supported on non-reducible MgO, the optimum molar metal composition Ni : Fe for CO_2 methanation was established to be 5 : 1. In accordance with previous reports on the promoting role of Fe for methanation, an increase in activity and CH_4 selectivity was observed, however, the selectivity around 10% at 350 °C was still low and the activity was not stable. An increased reaction order of H_2 and CO_2 in methanation with the addition of Fe further confirmed the promoting effect, which was not observed for the RWGS reaction.

2. The optimal ratio of Ni : Fe = 5 : 1 was further introduced to bimetallic Ni,Fe catalysts supported on CeO_2 and ZrO_2 and compared to monometallic counterparts to investigate the combined role of promoter and support effects for these two reducible oxides. CeO_2 was the most active support for both methanation and RWGS reactions, followed by ZrO_2, while MgO-supported bimetallic catalyst showed the lowest catalytic performance. This order corresponds to the reducibility of the supports suggesting metal-support interaction as origin of this effect. On these reducible supports, the presence of Fe even resulted in a bit lower methanation activity while the RWGS reaction was slightly promoted on both CeO_2 and ZrO_2 supported Ni, Fe catalysts. Therefore, different from the non-reducible MgO-supported catalysts, no promoting effect of Fe for methanation was observed on reducible oxides. This can be explained following the explanation of the promoting effect by Grundwaldt *et al.*, who proposed that the redox cycle of Fe at the surface of the Ni particles helps the CO_2 activation. In case of reducible oxides such as ZrO_2 or CeO_2 such activation of CO_2 can happen on oxygen vacancies of the support, and thus no promotion on the metal surface might be required. It was shown previously that oxygen vacancies and metal-zirconia interfacial sites can promote the activation of CO_2.[5,34,38] Such synergistic interplay of reduced oxide sites for CO_2 activation and metal sites for H_2 activation can also explain the superior stability of the catalysts supported on reducible oxides as no or less carbon species or oxygen-containing coupled products are present on the metal surface leading to deactivation by coking or oxidation.

3. ZrO_2-supported catalysts exhibited the highest CH_4 selectivity (94.4% on Ni/ZrO_2 at 350 °C). Instead of deactivation, they also showed a long activation period (~10 h) during reaction, consistent with the slow formation of oxygen vacancies due to the moderate reducibility. Also, the kinetic parameters were standing out from the other catalysts with regard to a very high activation energy and a strongly negative reaction order of H_2 for RWGS. In the context of our interpretation, this suggests that CO_2 competes with H_2 for the adsorption sites on the metallic Ni surface. Due to the hydrogen-rich feed stoichiometry, RWGS is inhibited by hydrogen and only little carbonaceous intermediates might be present on the Ni particles. The preferred CO_2 activation on the reduced support sites on the other hand does not lead to CO pathway on the metal sites likely proceeds *via* formate pathway on support sites with adjacent oxygen vacancies to form methane.[41,78]

4. The *in situ* DRIFTS results demonstrate that MgO, ZrO_2 and CeO_2 have a strong influence on Ni active sites. More specifically, there is a clear difference in the CO_{ad} species formed. The intensity ratio between carbonaceous/carbonates-like species and CO_{ad} bands on each sample after steady-state CO adsorption increased with increasing of the support reducibility (Fig. 12d), which can be interpreted as the Boudouard reaction is more promoted by the presence of oxygen vacancies. Such disproportionation will result carbon layer covered on Ni and prevent the formation of CO_{ad}. The other disproportionation product CO_2 will then be adsorbed on the support, which is consistent with our kinetic analysis. All these findings highlight MSI in reducible oxide-supported Ni-based catalysts, which can be addressed for the difference in their catalytic performance.

5. Conclusion

In conclusion, this study has shown that the well-established promotion effect of Fe on Ni-based catalysts with similar metal loading and metal particle size is present if non-reducible MgO is used as support, which according to literature report can be traced back to facilitated CO_2 activation involving Fe redox cycles. If reducible supports such as ZrO_2 and CeO_2 are involved, no such effect is evident. *In situ* DRIFTS with CO as probe and H_2-TPR as well as CO_2-TPD have demonstrated that the importance of MSI effect in these two supports, resulting into a new mechanism of CO_2 activation on the supports and rendering a promotion on the metal surface by Fe redundant. This hypothesis is consistent with the kinetic parameters reported here, which are most pronounced on Ni/ZrO_2, *i.e.* a large activation energy and a negative reaction order for H_2 in RWGS, while the pre-factor for methanation was still large. For these reasons, Ni/ZrO_2 reached the highest CH_4 selectivity of 94% at 350 °C, which is accompanied by an interesting activation behavior due to the dynamic nature of the under-lying MSI. The catalysts supported on the most reducible oxide CeO_2 with the richest oxygen vacancies showed the highest CO_2 methanation activity.

Data availability

The data supporting this article have been included as part of the ESI.†

Conflicts of interest

There are no conflicts to declare.

Acknowledgements

References

1 H. Blanco and A. Faaij, *Renewable Sustainable Energy Rev.*, 2018, **81**, 1049–1086.

2 X. Ning, R. Lin, R. O'Shea, D. Wall, C. Deng, B. Wu and J. D. Murphy, *iScience*, 2021, **24**, 102998.

3 A. Antenucci and G. Sansavini, *Renewable Sustainable Energy Rev.*, 2019, **100**, 33–43.

4 R. Estevez, L. Aguado-Deblas, F. M. Bautista, F. J. López-Tenllado, A. A. Romero and D. Luna, *Catalysts*, 2022, **12**, 1555.

5 H. Chen, H. Cui, Y. Lv, P. Liu, F. Hao and W. Xiong, *Fuel*, 2022, **314**, 123035.

6 R.-P. Ye, J. Ding, W. Gong, M. D. Argyle, Q. Zhong, Y. Wang, C. K. Russell, Z. Xu, A. G. Russell, Q. Li, M. Fan and Y.-G. Yao, *Nat. Commun.*, 2019, **10**, 5698.

7 L. Li, W. Zeng, M. Song, X. Wu, G. Li and C. Hu, *Catalysts*, 2022, **12**, 244.

8 N. Diyan Mohd Ridzuan, M. S. Shaharun, M. A. Anawar and I. Ud-Din, *Catalysts*, 2022, **12**, 469.

9 M. A. Aziz, A. A. Jalil, N. S. Hassan, M. Bin Bahari, A. H. Hatta, T. A. T. Abdullah, N. W. C. Jusoh, H. D. Setiabudi and R. Saravanan, *Process Saf. Environ. Prot.*, 2024, **186**, 1229–1241.

10 S. Chen and A. M. Abdel-Mageed, *Int. J. Hydrogen Energy*, 2023, **48**, 24915–24935.

11 E. Spennati, P. Riani and G. Garbarino, *Catal. Today*, 2023, **418**, 114131.

12 M. Tawalbeh, R. M. N. Javed, A. Al-Othman and F. Almomani, *Energy Convers. Manage.*, 2023, **279**, 116755.

13 J. Sehested, K. E. Larsen, A. L. Kustov, A. M. Frey, T. Johannessen, T. Bligaard, M. P. Andersson, J. K. Nørskov and C. H. Christensen, *Top. Catal.*, 2007, **45**, 9–13.

14 Y. Feng, L. Shen, W. Zhang, X. Yuan, M. Zhu and J. Xu, *J. CO2 Util.*, 2024, **80**, 102683.

15 A. I. Tsiotsias, N. D. Charisiou, I. V. Yentekakis and M. A. Goula, *Nanomaterials*, 2021, **11**, 28.

16 A. L. Kustov, A. M. Frey, K. E. Larsen, T. Johannessen, J. K. Nørskov and C. H. Christensen, *Appl. Catal., A*, 2007, **320**, 98–104.

17 Z. Bian, S. Das, M. H. Wai, P. Hongmanorom and S. Kawi, *ChemPhysChem*, 2017, **18**, 3117–3134.

18 T. Pu, J. Chen, W. Tu, J. Xu, Y.-F. Han, I. E. Wachs and M. Zhu, *J. Catal.*, 2022, **413**, 821–828.

19 J. Li, Q. Xu, Y. Han, Z. Guo, L. Zhao, K. Cheng, Q. Zhang and Y. Wang, *Sci. China: Chem.*, 2023, **66**, 3518–3524.

20 M.-A. Serrer, A. Gaur, J. Jelic, S. Weber, C. Fritsch, A. H. Clark, E. Saraçi, F. Studt and J.-D. Grunwaldt, *Catal. Sci. Technol.*, 2020, **10**, 7542–7554.

21 M.-A. Serrer, K. F. Kalz, E. SaraÒ‹i, H. Lichtenberg and J.-D. Grunwaldt, *ChemCatChem*, 2019, **11**, 5018–5021.

22 B. Mutz, M. Belimov, W. Wang, P. Sprenger, M.-A. Serrer, D. Wang, P. Pfeifer, W. Kleist and J.-D. Grunwaldt, *ACS Catal.*, 2017, **7**, 6802–6814.

23 A. B. Shirsath, M. L. Schulte, B. Kreitz, S. Tischer, J.-D. Grunwaldt and O. Deutschmann, *Chem. Eng. J.*, 2023, **469**, 143847.

24 H. L. Huynh, J. Zhu, G. Zhang, Y. Shen, W. M. Tucho, Y. Ding and Z. Yu, *J. Catal.*, 2020, **392**, 266–277.

25 B. Yan, B. Zhao, S. Kattel, Q. Wu, S. Yao, D. Su and J. G. Chen, *J. Catal.*, 2019, **374**, 60–71.

26 Z. Zhang, C. Shen, K. Sun, X. Jia, J. Ye and C.-J. Liu, *J. Mater. Chem. A*, 2022, **10**, 5792–5812.

27 W. K. Fan and M. Tahir, *J. Environ. Chem. Eng.*, 2021, **9**, 105460.

28 Q. Li, C. Wang, H. Wang, J. Chen, J. Chen and H. Jia, *Angew. Chem.*, 2024, **136**, e202318166.

29 C. Vogt, E. Groeneveld, G. Kamsma, M. Nachtegaal, L. Lu, C. J. Kiely, P. H. Berben, F. Meirer and B. M. Weckhuysen, *Nat. Catal.*, 2018, **1**, 127–134.

30 X. Zhou, G. A. Price, G. J. Sunley and C. Copéret, *Angew. Chem., Int. Ed.*, 2023, **62**, e202314274.

31 W. Gac, W. Zawadzki, M. Rotko, M. Greluk, G. Słowik and G. Kolb, *Catal. Today*, 2020, **357**, 468–482.

32 P. Frontera, A. Macario, M. Ferraro and P. Antonucci, *Catalysts*, 2017, **7**, 59.

33 L. P. Matte, A. S. Kilian, L. Luza, M. C. M. Alves, J. Morais, D. L. Baptista, J. Dupont and F. Bernardi, *J. Phys. Chem. C*, 2015, **119**, 26459–26470.

34 K. Larmier, W.-C. Liao, S. Tada, E. Lam, R. Verel, A. Bansode, A. Urakawa, A. Comas-Vives and C. Copéret, *Angew. Chem., Int. Ed.*, 2017, **56**, 2318–2323.

35 R. Ye, L. Ma, X. Hong, T. R. Reina, W. Luo, L. Kang, G. Feng, R. Zhang, M. Fan and R. Zhang, *Angew. Chem.*, 2024, **136**, e202317669.

36 Y. Ding, J. Chen, X. Lian, Z. Tian, X. Geng, Y. Wang, Y. Liu, W. Wang, M. Wang and Y. Xiao, *Appl. Catal., B*, 2024, **343**, 123508.

37 M. A. Abir, R. E. Phillips, J. Z. M. Harrah and M. Ball, *Catal. Sci. Technol.*, 2024, 4506–4521.

38 S. Kumari, A. N. Alexandrova and P. Sautet, *J. Am. Chem. Soc.*, 2023, **145**, 26350–26362.

39 S. Chen, A. M. Abdel-Mageed, C. Gauckler, S. E. Olesen, I. Chorkendorff and R. J. Behm, *J. Catal.*, 2019, **373**, 103–115.

40 Y. Bian, C. Xu, X. Wen, L. Xu, Y. Cui, S. Wang, C.-E. Wu, J. Qiu, G. Cheng and M. Chen, *Fuel*, 2023, **331**, 125755.

41 F. Arena, G. Italiano, K. Barbera, S. Bordiga, G. Bonura, L. Spadaro and F. Frusteri, *Appl. Catal., A*, 2008, **350**, 16–23.

42 M. Monai, K. Jenkinson, A. E. M. Melcherts, J. N. Louwen, E. A. Irmak, S. Van Aert, T. Altantzis, C. Vogt, W. van der Stam, T. Duchoň, B. Šmíd, E. Groeneveld, P. Berben, S. Bals and B. M. Weckhuysen, *Science*, 2023, **380**, 644–651.

43 C. Wei, H. Ding, Z. Zhang, F. Lin, Y. Xu and W. Pan, *Int. J. Hydrogen Energy*, 2024, **58**, 872–891.

44 F. Hu, C. Jin, K. H. Lim, C. Li, G. Song, Bella, T. Wang, R. Ye, Z.-H. Lu, G. Feng, R. Zhang and S. Kawi, *Fuel Process. Technol.*, 2023, **250**, 107873.

45 G. S. Dhillon, G. Cao and N. Yi, *Catalysts*, 2023, **13**, 1171.

46 W. L. Vrijburg, J. W. A. van Helden, A. Parastaev, E. Groeneveld, E. A. Pidko and E. J. M. Hensen, *Catal. Sci. Technol.*, 2019, **9**, 5001–5010.

47 M. Jafarbegloo, A. Tarlani, A. W. Mesbah, J. Muzart and S. Sahebdelfar, *Catal. Lett.*, 2016, **146**, 238–248.

48 L. Geng, B. Zheng, X. Wang, W. Zhang, S. Wu, M. Jia, W. Yan and G. Liu, *ChemCatChem*, 2016, **8**, 805–811.

49 Y. Wei, D. Luo, L. Yan, C. Ma, Z. Fu, L. Guo, M. Cai, S. Sun and C. Zhang, *Catal. Lett.*, 2022, **152**, 1835–1843.

50 C. Mebrahtu, S. Perathoner, G. Giorgianni, S. Chen, G. Centi, F. Krebs, R. Palkovits and S. Abate, *Catal. Sci. Technol.*, 2019, **9**, 4023–4035.

51 J. Li, J. Li and Q. Zhu, *Chin. J. Chem. Eng.*, 2018, **26**, 2344–2350.

52 D. Weber, T. He, M. Wong, C. Moon, A. Zhang, N. Foley, N. J. Ramer and C. Zhang, *Catalysts*, 2021, **11**, 1447.

53 C. Janke, M. S. Duyar, M. Hoskins and R. Farrauto, *Appl. Catal., B*, 2014, **152**, 184–191.

54 N. L. Visser, S. J. Turner, J. A. Stewart, B. D. Vandegehuchte, J. E. S. van der Hoeven and P. E. de Jongh, *ACS Nano*, 2023, **17**, 14963–14973.

55 P. Munnik, M. E. Z. Velthoen, P. E. de Jongh, K. P. de Jong and C. J. Gommes, *Angew. Chem.*, 2014, **126**, 9647–9651.

56 M. Mihaylov, K. Hadjiivanov and H. Knözinger, *Catal. Lett.*, 2001, **76**, 59–63.

57 M. Agnelli, H. M. Swaan, C. Marquez-Alvarez, G. A. Martin and C. Mirodatos, *J. Catal.*, 1998, **175**, 117–128.

58 N. Liu, J. Wei, J. Xu, Y. Yu, J. Yu, Y. Han, K. Wang, J. I. Orege, Q. Ge and J. Sun, *Appl. Catal., B*, 2023, **328**, 122476.

59 L. Li, B. Jiang, D. Tang, Z. Zheng and C. Zhao, *Catalysts*, 2018, **8**, 257.

60 W. Yu, Q. Zhou, H. Wang, Y. Liu, W. Chu, R. Cai and W. Yang, *J. Mater. Sci.*, 2020, **55**, 2321–2332.

61 X. Zhang, R. You, D. Li, T. Cao and W. Huang, *ACS Appl. Mater. Interfaces*, 2017, **9**, 35897–35907.

62 Y. Gao, R. Li, S. Chen, L. Luo, T. Cao and W. Huang, *Phys. Chem. Chem. Phys.*, 2015, **17**, 31862–31871.

63 W. Zheng, J. Zhang, Q. Ge, H. Xu and W. Li, *Appl. Catal., B*, 2008, **80**, 98–105.

64 T. Takeguchi, S.-N. Furukawa and M. Inoue, *J. Catal.*, 2001, **202**, 14–24.

65 C. Li, Y. Shi, Z. Zhang, J. Ni, X. Wang, J. Lin, B. Lin and L. Jiang, *J. Energy Chem.*, 2021, **60**, 403–409.

66 K. Chang, H. Zhang, M.-J. Cheng and Q. Lu, *ACS Catal.*, 2020, **10**, 613–631.

67 M. Carltonbird, S. Eaimsumang, S. Pongstabodee, S. Boonyuen, S. M. Smith and A. Luengnaruemitchai, *Chem. Eng. J.*, 2018, **344**, 545–555.

68 X. Li, X. Liu, J. Hao, L. Li, Y. Gao, Y. Gu, Z. Cao and J. Liu, *ACS Omega*, 2022, **7**, 24646–24655.

69 A. Parastaev, V. Muravev, E. Huertas Osta, A. J. F. van Hoof, T. F. Kimpel, N. Kosinov and E. J. M. Hensen, *Nat. Catal.*, 2020, **3**, 526–533.

70 L. R. Winter, E. Gomez, B. Yan, S. Yao and J. G. Chen, *Appl. Catal., B*, 2018, **224**, 442–450.

71 B. Miao, S. S. K. Ma, X. Wang, H. Su and S. H. Chan, *Catal. Sci. Technol.*, 2016, **6**, 4048–4058.

72 S. Chen, A. M. Abdel-Mageed, M. Li, S. Cisneros, J. Bansmann, J. Rabeah, A. Brückner, A. Groß and R. J. Behm, *J. Catal.*, 2021, **400**, 407–420.

73 X. Jia, X. Zhang, N. Rui, X. Hu and C.-J. Liu, *Appl. Catal., B*, 2019, **244**, 159–169.

74 Z. Cheng, B. J. Sherman and C. S. Lo, *J. Chem. Phys.*, 2013, **138**, 014702.

75 K. Lorber, J. Zavašnik, I. Arčon, M. Huš, J. Teržan, B. Likozar and P. Djinović, *ACS Appl. Mater. Interfaces*, 2022, **14**, 31862–31878.

76 N. Rui, X. Zhang, F. Zhang, Z. Liu, X. Cao, Z. Xie, R. Zou, S. D. Senanayake, Y. Yang, J. A. Rodriguez and C.-J. Liu, *Appl. Catal., B*, 2021, **282**, 119581.

77 T. Zhang, W. Wang, F. Gu, W. Xu, J. Zhang, Z. Li, T. Zhu, G. Xu, Z. Zhong and F. Su, *Appl. Catal., B*, 2022, **312**, 121385.

78 K. Li and J. G. Chen, *ACS Catal.*, 2019, **9**, 7840–7861.

79 J. I. Di Cosimo, C. R. Apesteguía, M. J. L. Ginés and E. Iglesia, *J. Catal.*, 2000, **190**, 261–275.

80 D. Wierzbicki, R. Baran, R. Dębek, M. Motak, T. Grzybek, M. E. Gálvez and P. Da Costa, *Int. J. Hydrogen Energy*, 2017, **42**, 23548–23555.

81 P. Summa, M. Gajewska, L. Li, C. Hu, B. Samojeden, M. Motak and P. Da Costa, *J. CO2 Util.*, 2022, **60**, 101983.

82 N. J. A. Rahman, A. Ramli, K. Jumbri and Y. Uemura, *Sci. Rep.*, 2019, **9**, 16223.

83 Z. Ni, X. Djitcheu, X. Gao, J. Wang, H. Liu and Q. Zhang, *Sci. Rep.*, 2022, **12**, 5344.

84 W. Liao, C. Tang, H. Zheng, J. Ding, K. Zhang, H. Wang, J. Lu, W. Huang and Z. Zhang, *J. Catal.*, 2022, **407**, 126–140.

85 Y. Wang, H. Ban, Y. Wang, R. Yao, S. Zhao, J. Hu and C. Li, *J. Catal.*, 2024, **430**, 115357.

86 S. Lin, Z. Li and M. Li, *Fuel*, 2023, **333**, 126369.

87 M. B. Jensen, L. G. M. Pettersson, O. Swang and U. Olsbye, *J. Phys. Chem. B*, 2005, **109**, 16774–16781.

88 D. Cornu, H. Guesmi, J.-M. Krafft and H. Lauron-Pernot, *J. Phys. Chem. C*, 2012, **116**, 6645–6654.

89 R. Ye, L. Ma, X. Hong, T. R. Reina, W. Luo, L. Kang, G. Feng, R. Zhang, M. Fan, R. Zhang and J. Liu, *Angew. Chem.*, 2024, **136**, e202317669.

90 Y. Yang, Z. Chai, X. Qin, Z. Zhang, A. Muhetaer, C. Wang, H. Huang, C. Yang, D. Ma, Q. Li and D. Xu, *Angew. Chem., Int. Ed.*, 2022, **61**, e202200567.

91 I. Hussain, G. Tanimu, S. Ahmed, C. U. Aniz, H. Alasiri and K. Alhooshani, *Int. J. Hydrogen Energy*, 2023, **48**, 24663–24696.

92 B. M. Tackett, E. Gomez and J. G. Chen, *Nat. Catal.*, 2019, **2**, 381–386.

93 A. Beck, D. Kazazis, Y. Ekinci, X. Li, E. A. Müller Gubler, A. Kleibert, M.-G. Willinger, L. Artiglia and J. A. van Bokhoven, *ACS Nano*, 2023, **17**, 1091–1099.

94 C. Ren, R. Yang, Y. Li and H. Wang, *Rev. Chem. Intermed.*, 2019, **45**, 3019–3032.

95 G. Martra, F. Arena, M. Baricco, S. Coluccia, L. Marchese and A. Parmaliana, *Catal. Today*, 1993, **17**, 449–458.

96 K. I. Hadjiivanov and G. N. Vayssilov, in *Advances in Catalysis*, Academic Press, 2002, 47, pp. 307–511.

97 G. Busca and V. Lorenzelli, *Mater. Chem.*, 1982, **7**, 89–126.

98 S. Chen, T. Cao, Y. Gao, D. Li, F. Xiong and W. Huang, *J. Phys. Chem. C*, 2016, **120**, 21472–21485.

99 S. Chen, L. Luo, Z. Jiang and W. Huang, *ACS Catal.*, 2015, **5**, 1653–1662.

100 M. B. Jensen, S. Morandi, F. Prinetto, A. O. Sjåstad, U. Olsbye and G. Ghiotti, *Catal. Today*, 2012, **197**, 38–49.